AIChE WILEY InterScience DISCOVER SOMETHING GREAT

Vortex Tracking and Mixing Enhancement in Stirred Processes

A. Ducci and M. Yianneskis
Experimental and Computational Laboratory for the Analysis of Turbulence (ECLAT), Division of Engineering, King's College London, Strand WC2R 2LS, U.K.

DOI 10.1002/aic.11076
Published online January 2, 2007 in Wiley InterScience (www.interscience.wiley.com).

The precession of macroinstability (MI) vortices in stirred vessels has been investigated with vortex tracking methodologies, and utilized to enhance mixing performance. The techniques used are presented and employed to determine the instantaneous and average location, size and vorticity of the MI vortex for Re = *3,200 and 32,000 in 80 and 294 mm dia. vessels stirred by a Rushton impeller. Measurements of mixing time are performed in a 588 mm dia. vessel with surface insertion of a passive scalar tracer either inside or outside the precessing MI vortex. The data indicate that in-vortex insertion can result in a mixing time reduction of 20%, and even possibly 30%.* © 2007 American Institute of Chemical Engineers *AIChE J,* 53: 305–315, 2007

Introduction

The occurrence of vortical flows in many engineering apparatuses presents opportunities, as well as challenges for the design of processes involving mixing of different fluids. The dissipative nature of vortical flows makes them prime candidates to be utilized to enhance mixing in stirred processes. On the other hand, if such flows are not taken into account in the design of a mixing process, not only the energy expended in their generation is not utilized, but also the mixing characteristics may be undesirably different to those intended by the designer.

The two main vortical structures encountered in stirred vessels are the trailing vortices emanating from the turbine blades,[1,2,3,4,5] and the precessing and other kinds of macroinstabilites.[6,7] The former are relatively well studied and are known to be responsible for the dissipation of a substantial proportion of the energy input to a stirred vessel.[8,9] The characterization of MIs has received much attention in recent years, for example,[10,11,12] but their effect on mixing effectiveness has not been studied so far.

Although mixing processes that encompass chemical reactions involve primarily molecular level processes that clearly are influenced in a direct manner only by mixing at such a level (micromixing), the development of such processes is nevertheless indirectly affected by mixing at the larger scales (macromixing), for instance by transporting reactants through parts of a stirred reactor, where the turbulence characteristics and/or chemical composition may vary substantially. In particular, low-frequency high-amplitude oscillatory motions in regions of low-turbulence in stirred vessels, such as MIs, have the potential of transporting substances fed to a mixing process over long distances.[13]

Macroinstabilities (MIs) involve flow motions that can be instigated by different flow properties and various types of MIs are encountered in fluid flows. An example of a macroinstability is that in a convectively unstable system: for certain temperature gradients internal gravity waves can grow to large amplitude and cause a large-scale convection of the fluid, which tends to reduce the temperature gradient. Other examples are the Rayleigh-Jeans instability, in which a denser fluid is supported by a less dense fluid, and the Kelvin-Helmholtz instability, in which one fluid flows over another, such as wind over water, causing surface waves to grow. Another example in rotating (swirling) flows is the precessing vortex core (PVC). Such MIs can be utilized for the improvement of performance of many technological devices, for example, in swirl combustion chambers. In swirling flow fields with a PVC the unsteadiness due to the MI can account for up to 70% of the total energy of the ensemble-averaged velocity fluctuations.[14]

In vessels stirred by Rushton impellers a similar precessional-type of MI has been identified,[6] and found to move around the shaft axis with a nondimensional frequency $f' = f/N = 0.106$ for $400 \leqslant$

Correspondence concerning this article should be addressed to M. Yianneskis, at michael.yianneskis@kcl.ac.uk.

© 2007 American Institute of Chemical Engineers

$Re \leqslant 6{,}300$, and $f' = 0.02$ for $13{,}600 \leqslant Re \leqslant 54{,}000$, while for $6{,}300 \leqslant Re \leqslant 13{,}600$ both frequencies were present in the flow.[15]

Related phenomena in relatively simple flow geometries such as cylindrical rotor-stator cavities have been widely studied and exhibit similarities with MIs in stirred vessels; for example, it has been reported that at low Re the flow undergoes a transient before attaining a purely periodic behavior of low nondimensional frequency $f' = 0.113$,[16] that is very similar to the 0.106 value previously reported for low Re flows in stirred tanks.[15] Similarly, the linear variation of the vortex frequency with flow rate in swirling flows[17] is akin to that observed in stirred vessels, where f varies linearly with N.

The complexity of the three-dimensional (3-D) turbulent flows in stirred vessels makes understanding of the MIs encountered a most demanding task, calling for the use of complex techniques not easily translated into an industrial environment. Recently, however,[12] demonstrated that the presence of the MI vortices could be detected with a pressure transducer that offers a simple and inexpensive means to locate the vortex passage through a particular radius in the vessel. This development opened up opportunities to utilize the vortex in mixing practice and provided motivation for the present work in which 2-D PIV, and 2-point LDA are employed to improve fundamental understanding of the underlying physics of MI vortices. Through tracking of the MI vortex, knowledge of the instantaneous and average vortex size, location and vorticity has been obtained in this work. Such information is used in turn to guide surface tracer insertion into the vessel, and the effect of *in vortex* insertion on mixing time, and, hence, on mixing performance is assessed. The data reported below indicate clearly that a considerable reduction in mixing time and hence energy input can be possible if tracer insertion is synchronized with the vortex passage.

Flow Configuration and Experimental Apparatus

This study was planned in three successive stages, with three sets of experiments carried out to investigate different vortex properties. In the first stage, the time-resolved and ensemble averaged characteristics of the MI in the $r - z$ plane were estimated using a 2-D PIV. In the second stage, 2-point LDA experiments were carried out to determine the inclination of the vortex axis in the $z - \theta$ plane. In the third stage the objective was to assess the mixing efficiency of the tank when a passive scalar is inserted in the core of the vortex. A sketch of the MI vortices present above and below the impeller for a high Re regime is provided in Figure 1: they constitute two whirlpool-like vortices extending from the impeller to the top/bottom of the vessel, and precessing around the vessel axis.

In the first stage a 2-D PIV system was employed to assess the precession of the MI vortex around the vessel axis for $Re = 3{,}200$ and $Re = 32{,}000$. The mixing vessel dia. $T = 294$ mm, was equal to the vessel height, and had four equispaced baffles of width $T/10$ and thickness $T/100$. The six-blade Rushton turbine of dia. $D = T/3$ was set to a height $C = T/2$. This configuration was selected to obtain well defined MI vortices of similar intensity both above and below the impeller.[6]

A 13 kHz time-resolved Dantec camera was positioned underneath the rig and focused through a window present at the bottom of the vessel on the horizontal laser sheet (that is, in the $r - \theta$ plane) alternatively located at $z/T = 0.15, 0.25, 0.35, 0.43$ (where $z/T = 0$ corresponds to the bottom of the vessel). To minimize statistical errors four sets of 1,021 frames were recorded for each axial position investigated, with frame-rates of 40 Hz, and 70 Hz for $Re = 3{,}200$ and $Re = 32{,}000$, respectively. The frame rates were selected in order to obtain a complete precession of the MI around the vessel axis in the time required to record a single set (that is, 1,021 frames). Considering the large-scale structures to be investigated, the interrogation area (32×32 pixels with 50% cell overlapping) was relatively large with sides approximately equal to $0.014\ D$. To record a complete precession of the MI around the vessel axis, the center of the area investigated was positioned approximately on the axis of the vessel, and its side was comparable to the impeller dia. D. In this respect it should be pointed out that the camera was fixed, and, therefore, the size of the area investigated changed for different planes of focus, with larger investigation areas for axial positions further away from the camera ($z/T = 0.43$), and smaller for closer ones ($z/T = 0.15$).

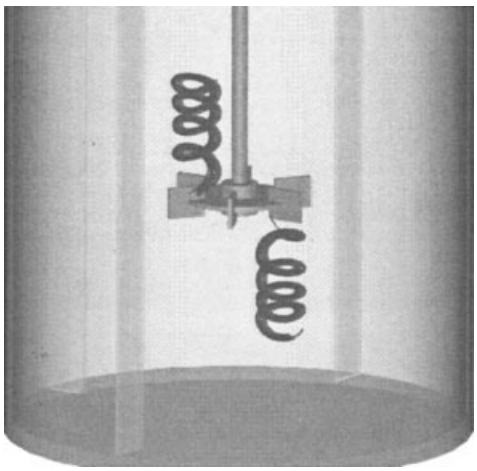

Figure 1. Top and bottom MI vortices for a high *Re* range regime.

A similar configuration but with a scaled down vessel and impeller ($T = 80$ mm) was used in the second stage, when 2-point LDA experiments were carried out to estimate the variation of the correlation coefficient $R_{\theta\theta}$, of the tangential velocity component, U_θ, for two points displaced by Δz. In this case the first probe was kept at a fixed axial position $z/T = 0.31$, while the second probe was alternatively moved along six axial positions both below, $z/T = 0.312$; 0.375; 0.437, and above, $z/T = 0.562$; 0.625; 0.687, the impeller. The radial coordinate of the two probes was $r/T = 0.08$. Similarly to the first stage of study the LDA experiments were carried out for $Re = 32{,}000$ and $Re = 3{,}200$.

A standard two-channel Dantec LDA was used with the two probes arranged in the configuration already reported in,[9,18] where 2-point LDA measurements were carried out to estimate the dissipative length scales in a grid generated turbulent flow, and in the impeller stream of a Rushton turbine, respectively. It should be noted however that in the present study a high-spatial resolution system was not required as in the aforementioned works, since the MIs are large scale structures. Both probes operated in backscatter (that is, no side scatter mode as in 9, to reduce the control volume size), with control volumes of size $0.03 \times 0.03 \times 0.24$ mm^3 and $0.05 \times 0.05 \times 0.3$ mm^3. The two probes entered the vessel in the vertical (that is, $r - z$) plane midway

between two adjacent baffles, and a trough was used to minimize the distortion due to the refraction at the cylindrical vessel wall. The liquid surface was contained by a lid.

The third set of experiments aimed at investigating the variation of the mixing time θ, when the insertion of a passive scalar was made inside and outside of the MI vortex core. To facilitate the manual tracer insertion in the vortex core, a reduction of the precessional frequency of the MI vortex for a given *Re* was necessary, and, therefore, a scaled up vessel with $T = 588$ mm was selected. The tank water height was set to $H = 440$ mm ($H/T = 0.75$) for this experiment. This selection was necessitated by the need to visualize the MI vortex clearly in order to proceed with the insertion. Under this condition the presence of the vortex was visualized by the air sucked in the vortex core. The rotational speed of the impeller was $N = 70$ rpm. Similarly to the previous experimental stages the impeller clearance was kept at $C = 0.5\ T$, but it has to be remarked that in this case the distance between the free surface, and the impeller was smaller than the distance between the impeller and the bottom of the vessel.

Similarly to the early work of[19], and the more recent studies of[20] and,[21] a conductivity probe was used to record the variation of local conductivity when a 7 mL solution of distilled water saturated with potassium cloride (KCl) was inserted in the tank. The solution was introduced by means of a syringe with an insertion time of approximately 1 s. To reduce the momentum along the z axis created by the syringe, a 90° bent tubing was attached at the exit of the syringe as to have a horizontal insertion with respect to the water-free surface. It should be noted that the present study aimed at investigating the difference in mixing times when the passive scalar was introduced inside or outside of the MI vortex, and, therefore, calibration of the conductivity and the concentration was not necessary.

For all the experiments described the working fluid used was water and in the first and second stages of the work 10 μm silver coated hollow particles were used to seed the water. It should also be remarked that although three different vessel sizes were employed for the different experiments reported here, the vessels were geometrically precisely scaled. It has been previously established that, for single-phase flow, the mean flow and turbulence quantities measured in vessels stirred by Rushton impellers scale well when normalized with appropriate scaling factors such as V_{tip}: ${V_{tip}}^2$: and so on, provided that scaling of all geometrical features, including the blade thicknesses, is taken into account.[22] showed that in a 294 mm vessel differences of scaled quantities were only present when the *Re* was low, and the near-impeller flow was not fully turbulent, while[23] found near-identical normalized values for turbulent flow for different vessel sizes.

Unless directly stated, in the remainder of this article a cylindrical coordinate system (r, θ and z) with origin in the center of the base of the vessel will be used. Details of the processing techniques employed to analyse the different experimental data are provided in the following section.

Results and Discussion

In the following sub-sections the three parts of the investigation, that is, vortex tracking and identification, MI vortex axis, and mixing time experiments are discussed in sequence. In brief, the rationale for the selection of these three parts of the work was to identify the vortex location and size, to establish the shape of the vortex axis to see whether enhanced convection of tracer to the impeller (intense mixing) region was likely, and to quantify any such enhancement through mixing time measurements, respectively.

Vortex identification and tracking

In this section, only a brief description of the identification and tracking methodology is provided, but an exhaustive review of the related processing procedure can be found in[24] where the technique has been assessed against more conventional processing approaches, such as spectral, autocorrelation and spatial correlation analyses, that are commonly employed in literature to identify periodicities in a flow. The processing procedure was designed in two successive stages; the objective of the first stage was to identify the vortex core and its characteristics in each single frame, while the second stage was developed to track the path of the vortex center through different frames (instances).

The first stage comprised applying the λ_2 technique proposed by[25], who compared different methodologies to identify a vortex core (see also[26]). It should be noted that λ_2 is the second highest eigenvalue of the $S^2 + \Omega^2$ tensor, (where S_{ij} and Ω_{ij} are the normal/shear strains $S_{ij} = \frac{1}{2}\left(\frac{\partial U_i}{\partial x_j} + \frac{\partial U_j}{\partial x_i}\right)$, and the rotation of the fluid particle $\Omega_{ij} = \left(\frac{1}{2}\frac{\partial U_i}{\partial x_j} - \frac{\partial U_j}{\partial x_i}\right)$, respectively) and, under the assumptions of *(1)* negligible unsteady strains of the fluid particle; and *(2)* negligible viscous effects; it is equal to the second derivative of the pressure in the corresponding eigenvector direction (that is, $-\rho^{-1}\partial^2 p/\partial {x_2}^{*2}$). As shown by[25] a negative value of λ_2 (and, therefore, also of λ_3 which is the lowest eigenvalue) implies that a vortex core associated to a low-pressure zone is present in a generic plane oriented normally to the direction of the first eigenvector (that is, the one corresponding to λ_1).

The vortex border was identified by a combined set of conditions [24] made both on the level and sign of the average vorticity on the border, as well as on the value of λ_2. Once the border of the vortex was determined, the center coordinates (C_{xi}) were calculated using the vorticity weighted average proposed by[27]. The velocity vector and vorticity contour plot of a generic frame is shown in Figure 2. In this case it is possible to see how the

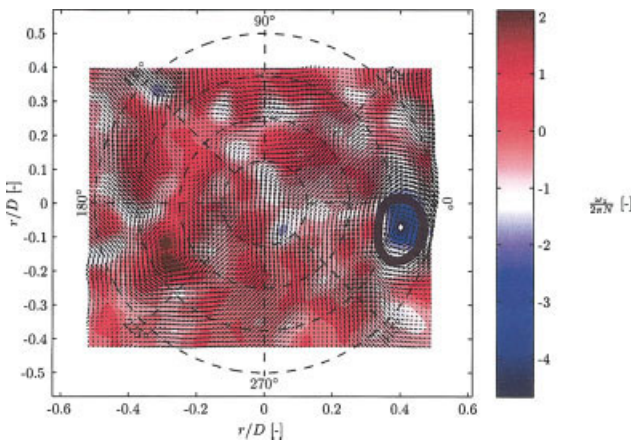

Figure 2. ω_z/N contour plot and velocity vector plot for the $z/T = 0.25$ horizontal plane; the MI vortex center and border are identified by the white diamond symbol and the thick black line, respectively (*Re* = 32,000).

[Color figure can be viewed in the online issue, which is available at www.interscience.wiley.com.]

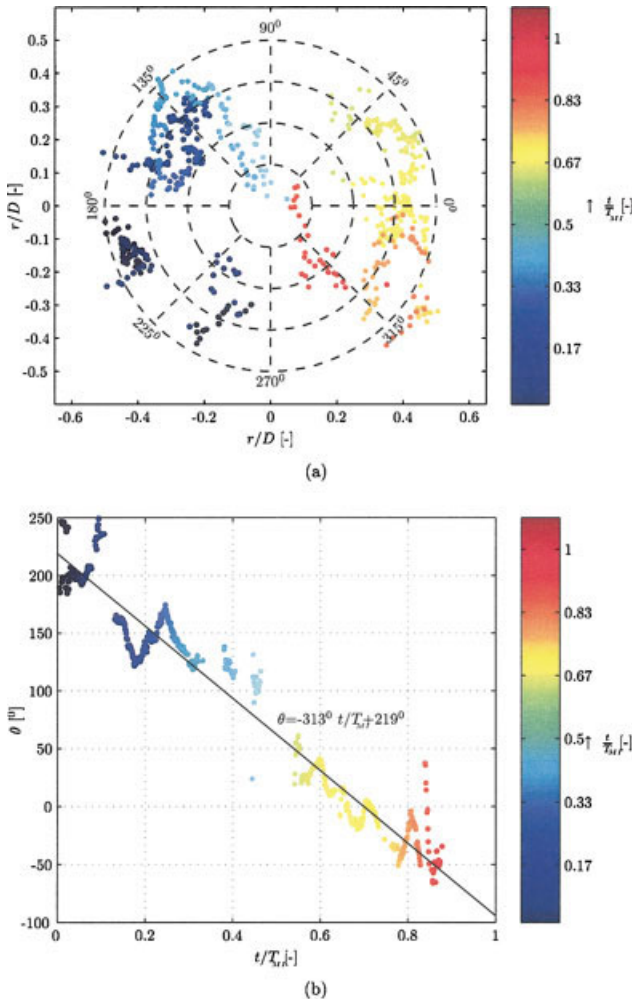

Figure 3. Instantaneous variation of the angular position assumed by the MI vortex with time during a single vortex revolution around the shaft for *Re* = 32,000; (a) plan view showing successive radial positions of the vortex center; and (b) variation of circumferential coordinate, θ, of the vortex center with time.

[Color figure can be viewed in the online issue, which is available at www.interscience.wiley.com.]

methodology proposed determined correctly the vortex corresponding to the MI. Once the vortex center and border are known, any other characteristic such as the total MI vorticity, the maximum MI vorticity, size, and so on, can be easily calculated.

As previously mentioned the second issue to be tackled was to track the path of the MI vortex through the different frames. The difficulty of this task was mainly due to the fact that the MI does not precess around the vessel axis in a continuous way, but tends to disappear after some time and reappear somewhere else in proximity of the last position detected. It was, therefore, necessary to put some conditions on the life of the vortex for each single appearance interval, and track its path for each interval.[24]

The results obtained for $Re = 32{,}000$ are reported in Figure 3 where the variation with time of the positions assumed by the MI vortex is represented. As shown by the arrow next to the colorbar, an increase of time corresponds to circles of hues varying from blue to red. It should be noted that the time t elapsed from the beginning of the experiment is nondimensionalized with a period $T_{MI} = 1/(0.02N)$, where, in agreement with previous finding (see for example[15]), the MI is assumed to precess around the vessel axis with a frequency $f = 0.02N$.

Despite the zig-zag path followed by the MI and the difficulty in determining the position of MI for each single frame (that is, some circles corresponding to certain hues are missing), it is evident from Figure 3a that the MI precesses around the vessel axis. From Figure 3b the actual precessional frequency of the MI f, for this case can be estimated from the slope of the straight line fitted through the different angular positions. It can be readily shown that the actual precessional frequency of the MI is $f/(N) = (313°/360°)\ 0.02 = 0.0174$, which is very close to the value of 0.02 previously cited. Similar small discrepancies can be found when comparing data present in literature, see for example the fre-

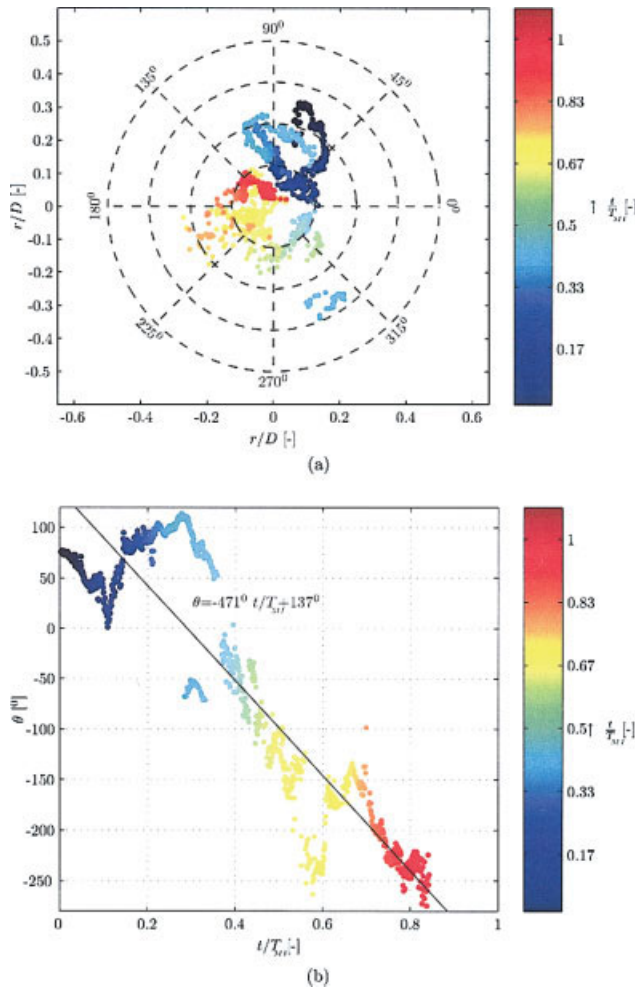

Figure 4. Instantaneous variation of the angular position assumed by the MI vortex with time during a single vortex revolution around the shaft for *Re* = 3200; (a) plan view showing successive radial positions of the vortex center and (b) variation of circumferential coordinate, θ, of the vortex center with time.

[Color figure can be viewed in the online issue, which is available at www.interscience.wiley.com.]

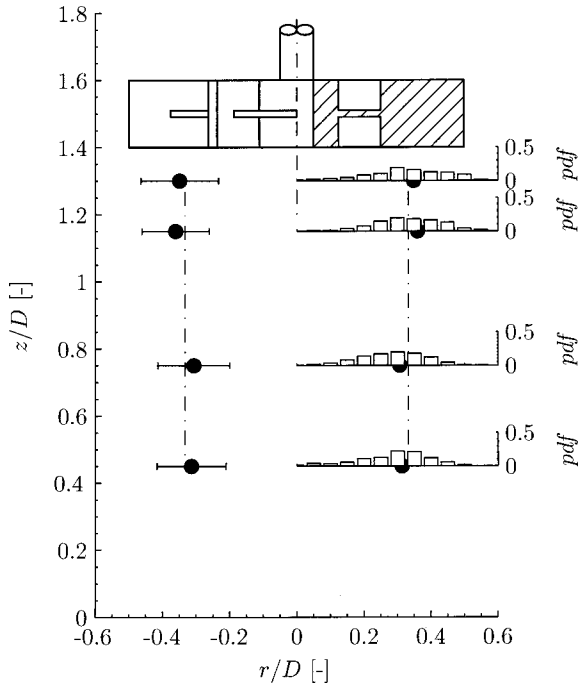

Figure 5. Projection of the MI axis on the $r - z$ plane for *Re* = 32,000; Inset diagrams on the RHS: probability density function of the radial coordinate of the vortex center, *r/D,* for different axial positions; inset diagrams on the LHS: ensemble averaged vortex diameter $2\bar{\rho}/D$, for different axial positions.

quency obtained by[6,15], and[7]. Differences in the f values reported in earlier works have been attributed primarily to the difficulties of determining precisely low-frequencies with spectral analysis methods. In addition, the present f data correspond to a single MI cycle, whereas in earlier works averages over many cycles were obtained. In future works the likelihood of f variations over many cycles will be ascertained, but near identical fs were found from the various repeats of the present experiments over single MI cycles.

Similar results corresponding to $Re = 3{,}200$ are shown in Figure 4. In this case the precession of the MI around the vessel axis is also clear. However, the actual MI frequency (0.13 N) is slightly higher than the one obtained in previous studies for low Re's (that is, 0.106 N). From a qualitative comparison between the data ($z/T = 0.15$) shown in Figure 3a and Figure 4a, it is possible to conclude that for higher Re the MI tends to spend more time in radial positions further away from the vessel axis than it does for lower Re values.

As already discussed in the introduction sec 1, the motivation behind this work is to improve large-scale mixing efficiency by providing guidance for an optimal position of the feeding pipe in order to fully exploit the suction present in the MI vortex core. In this respect, an estimate of the pressure drop present in the MI vortex might be relevant to calibrate a pressure transducer that could be used to activate the feeding pipe. From this point of view Δp can be estimated from the double integral of the λ eigenvalues $\left(\lambda_i = -\frac{1}{\rho}\frac{\partial^2 p}{\partial x_i^{*2}}\right)$ along the associated eigenvector directions, x_i*. The pressure drops associated to the MI vortex shown in Figure 2 were 20–25 Pa (that is, $\Delta p/(0.5\rho V_{tip}{}^2) = 0.038$–$0.048$). Taking into account the different turbine employed by[12], the estimated pressure drop compares reasonably well with the one they measured directly with a pressure transducer that was fixed to the vessel wall ($\Delta p = 10$ Pa; $\Delta p/(0.5\rho V_{tip}{}^2) = 0.023$). From this point of view it should be noted that with a pressure drop of 25 Pa the fluid entrained in the vortex is accelerated along the vortex axis (that is, in the axial direction) to a velocity of around 0.25 V_{tip}, which is 2.5 times higher than the local axial mean velocity $\overline{U_z}$ ($\approx 0.1\ V_{tip}$ at $z/T = 0.25$, $r/T = 0.13$).

MI vortex axis

The variations of the ensemble averaged radial coordinate r/D, of the vortex center, and of its nondimensional diameter, $2\bar{\rho}/D$, with the different axial locations examined are shown in Figures 5 and 6 for $Re = 32{,}000$ and $Re = 3{,}200$, respectively. Considering the righthand side (RHS) of Figure 5 it is possible to see that the MI vortex axis is almost vertical in the $z - r$ plane. However, the large standard deviation of the vortex centers, evident from the probability density distributions shown in the inset diagrams, gives a clear indication of the comparatively large area underneath the impeller that is swept by the MI vortex during its precession around the vessel axis. Maximum and minimum radial coordinates r/D, of 0.55 and 0.05 are almost equally likely to happen (although far less likely than locations nearer the vortex axis) for all the axial planes investigated. In this respect it is worth to point out that almost all the

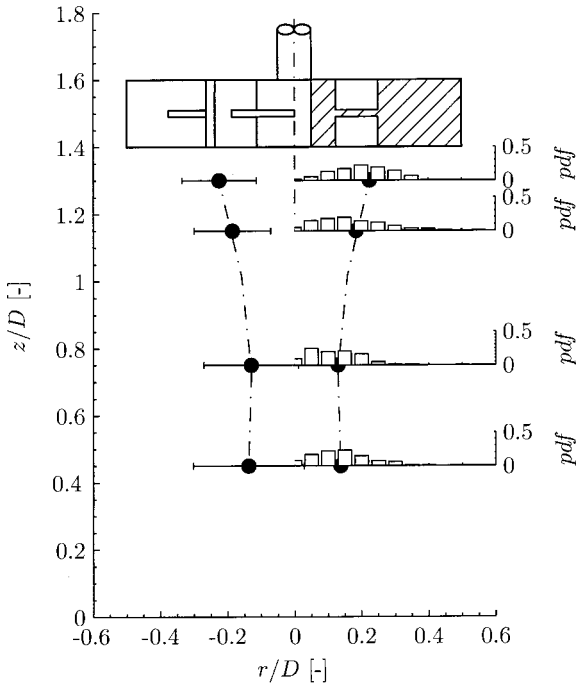

Figure 6. Projection of the MI axis on the $r - z$ plane for *Re* = 3,200; inset diagrams on the RHS: probability density function of the radial coordinate of the vortex center, *r/D,* for different axial positions; inset diagrams on the LHS: ensemble averaged vortex diameter $2\bar{\rho}/D$, for different axial positions.

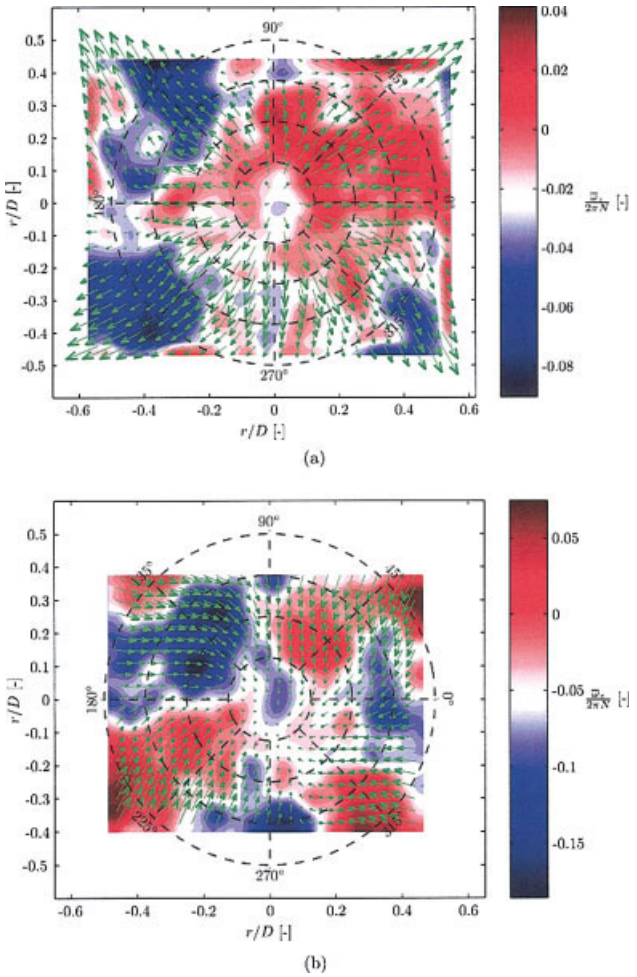

Figure 7. Velocity vectors and vorticity contour plots of the ensemble averaged flow field for different horizontal planes, *z/D* (*Re* = 32,000): (a) *z/D* = 1.3 and (b) *z/D* = 0.45.

[Color figure can be viewed in the online issue, which is available at www.interscience.wiley.com.]

pdf's are negatively skewed, indicating that the center of the vortex is spending more time in radial coordinates in the mid-upper range of the pdf, with fewer occurrences in the lower end range of the radial positions shown. The ensemble averaged variation of the MI dia. $2\bar{\rho}$, shown in the lefthand side (LHS) of Figure 5 is almost constant for all the axial positions examined and approximately equal to 0.2 D.

The interpolation of the MI vortex axis from the ensemble averaged estimates of the vortex centers at different axial positions z/D is shown in Figure 6 for $Re = 3{,}200$. The shape of the axis is complex with the axis radius decreasing nonlinearly with decreasing z/D. This shape however reflects the characteristics of the bulk flow field of the bottom part of the vessel that is discussed later in this section. Contrary to the data shown for $Re = 32{,}000$, in this case the vortex center pdf's shown in the inset diagrams in the RHS of Figure 6 are positively skewed, with a higher probability of the vortex center being in the low-mid range of the distribution, and with fewer occurrences in the upper end range. Similarly to the radial coordinate of the center, r/D, the radius of the MI vortex also changes considerably for the different axial positions investigated. Considering the LHS of Figure 6 it is possible to see that the vortex almost doubles in size as z/D varies from 1.3 to 0.45 with $\bar{\rho}/D = 0.1$ and $\bar{\rho}/D = 0.175$, respectively.

The ensemble averaged characteristics of the mean velocity flow field in stirred vessels have been extensively studied in literature, and the present PIV data obtained in the bulk flow region underneath the impeller confirm the double circulation loops present above and below the impeller already outlined in the works of[2,28,29,30], to mention but a few. Considering Figures 7a and b relative to the axial positions $z/D = 1.3$ and $z/D = 0.45$, respectively, for $Re = 32{,}000$, the expected flow pattern is evident with outwards radial flow for the higher-plane considered, corresponding to the upper part of the bottom circulation loop, and inwards radial flow for the lower one, corresponding to the lower part of the bottom circulation loop. To improve the readability of Figures 7a and b, only a limited number of vectors have been plotted with a distance between two adjacent vectors being three times longer than the side of the interrogation cell. It should be stressed that the vector scaling factor in Figures 7 and 8 is different to that in Figure 2. It is worth noting that in both figures the intensity of the tangential velocity is significantly smaller than the radial one.

The plot of the mean velocity flow field ($z/D = 1.3$) for the lower flow regime, $Re = 3{,}200$, investigated is shown in Figure 8. A comparison with the plots already discussed for the higher Re investigated, indicates an evident change in flow pattern with a large area centered around the vessel axis, that is dominated by the tangential velocity component. This behavior was evident in all axial locations investigated with the region of solid body rotation gradually decreasing in size with decreasing z/D. From Figure 8 it emerges that this region of solid body rotation is the driving mechanism that determines the MI vortex precession velocity.

From a physical point of view the difference in flow patterns for the two Re investigated can be explained by considering that for the lower Re the solid body rotation region is determined by

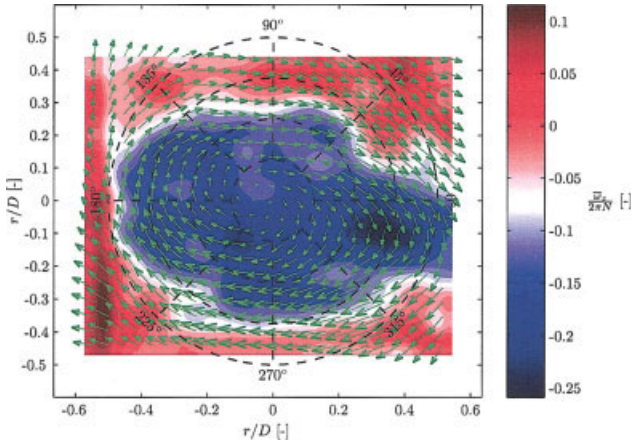

Figure 8. Velocity vectors and vorticity contour plots of the ensemble averaged flow field for *z/D* = 1.3 (*Re* = 3,200).

[Color figure can be viewed in the online issue, which is available at www.interscience.wiley.com.]

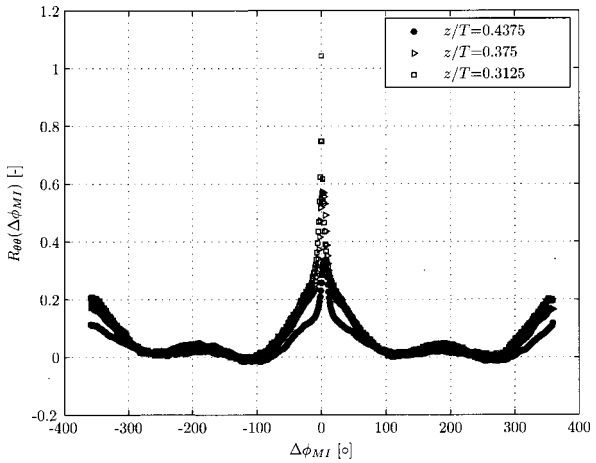

Figure 9. Variation of the correlation coefficient $R_{\theta\theta}$ with phase-lag angle $\Delta\phi_{MI}$ for three different axial positions of the adjustable probe below the impeller (Re = 32,000); ●: z/T = 0.437; ▷: z/T = 0.375; □: z/T = 0.312.

the viscous stresses, due to the rotation of the impeller disc and blades, acting on the fluid below the impeller. When Re is increased to 32,000 the inertial forces due to the impeller jet are dominant, resulting in a lower and upper circulation loops that extend closer to the vessel axis ($r/T = 0$).

The change of the mean flow pattern inevitably affects the precession of the MI vortex, and could be the reason for the difference in precessing frequency f' found for the ranges of $Re \leqslant 6{,}300$ and $Re \geqslant 13{,}600$[7]. Taking into account the radial position r, assumed by the center of the vortex for each axial plane investigated, it was possible to determine the parameter $U_\theta/2\pi rN$ which can provide an estimate of f/N (that is, $U_\theta/2\pi rN = \omega r/(2\pi rN) \approx 2f\pi/(2\pi N)$ where ω is the angular speed of the solid-body rotation). The average of the four estimates of f/N were equal to 0.16 and 0.022 for $Re = 3{,}200$ and $Re = 32{,}000$, respectively. Despite the higher estimation of f/N for the low Re case (from a frequency spectrum analysis f/N should be closer to 0.106), this analysis confirms the findings of [7] and can provide a reasonable explanation of the order of magnitude difference between the characteristic precessional frequencies in the lower and upper ranges of Re.

The 2-point LDA experiment data were processed with the conditional sampling method previously implemented by.[31] This methodology exploits the cyclical nature of the flow due to the precession of the MI vortex, and consists of a phase resolved analysis of the velocity signal of the two LDA probes, where the phase angle ϕ_{MI}, defined in Eq. 1, accounts for the extent of revolution of the MI around the vessel axis

$$\phi MI_i = (t_i/T_{MI}) \times 360^\circ \tag{1}$$

In Eq 1 t_i and T_{MI} are the arrival time of the i_{th} sample, and the period taken by the MI to precess around the vessel axis, respectively. It should be noted that in the rest of the discussion a value of $1/(0.02N)$ and $1/(0.1N)$ was given to the period T_{MI} for $Re = 32{,}000$ and $Re = 3{,}200$, respectively. Once the angle ϕ_{MI} is estimated for all the particles that crossed the two control volumes at different times, it is possible to determine the variation of the correlation coefficient $R_{\theta\theta}(\Delta\phi_{MI})$ with phase lag $\Delta\phi_{MI}$ between the velocity records obtained at two different axial positions Δz. The definition of the correlation coefficient $R_{\theta\theta}(\Delta\phi_{MI})$ is shown in Eq. 2

$$R_{\theta\theta}(\Delta z, \Delta\phi_{MI}) = \frac{\overline{u_\theta(z_0, \phi_{MI_0}) u_\theta(z_0 + \Delta z, \phi_{MI_0} + \Delta\phi_{MI})}}{u'_\theta(z_0, \phi_{MI_0}) u'_\theta(z_0 + \Delta z, \phi_{MI_0} + \Delta\phi_{MI})} \tag{2}$$

where the average is made only between the velocities of those particles that crossed the two control volumes with a phase lag $\Delta\phi_{MI}$. The phase lag, $\Delta\phi_{MI}$, is defined as the difference between the angle $\phi_{MI_{\Delta z}}$ of the adjustable probe, and the angle ϕ_{MI_0} of the fixed one (that is, $\Delta\phi_{MI} = \phi_{MI_{\Delta z}} - \phi_{MI_0}$).

The variations of the correlation coefficient $R_{\theta\theta}(\Delta\phi_{MI})$ with phase lag $\Delta\phi_{MI}$ for the axial positions z/T assumed by the adjustable probe below and above the impeller are shown in Figures 9 and 10, respectively. Both figures refer to $Re = 32{,}000$. As expected, the correlation coefficient exhibits a maximum for $\Delta\phi_{MI} = 0$ and $\Delta z = 0$, when the two probes are aligned in the same point of coordinate $z/T = 0.31$ (see Figure 9). As the adjustable probe is moved away from the fixed one, the maximum of the correlation coefficient gradually decreases with values around 0.6 and 0.4 for $z/T = 0.375$ and $z/T = 0.4375$, respectively. However, the maximum position of $R_{\theta\theta}$ does not vary (that is, $\Delta\phi_{MI} = 0$) with increasing axial coordinate of the adjustable probe, implying that the MI vortex influences in the same way, at the same time, the flow pattern at two different axial locations. This leads to the conclusion that the MI axis is vertical throughout its precession and parallel to the line joining the different axial positions investigated.

The variation of $R_{\theta\theta}$ with $\Delta\phi_{MI}$ for axial positions of the adjustable probe above the impeller is shown in Figure 10. As already pointed out by[31] the maximum of $R_{\theta\theta}$ is located at an angle $\Delta\phi_{MI} \approx \pm 180^\circ$ implying that the MI vortices present above and below the impeller are radially positioned opposite to each other during their precession around the axis (see also the sketch in Figure 1). Similarly to the comments already made for the mea-

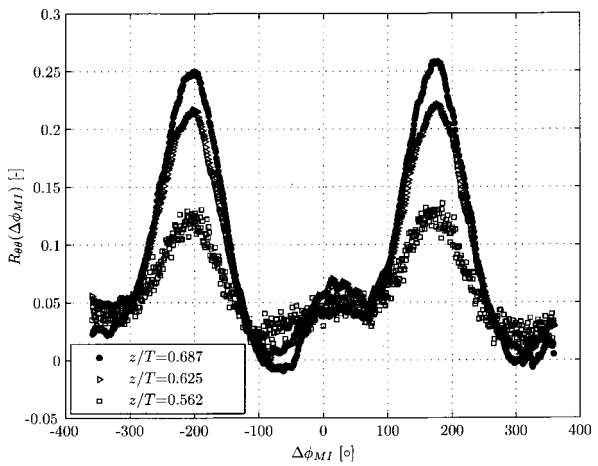

Figure 10. Variation of the correlation coefficient $R_{\theta\theta}$ with phase-lag angle $\Delta\phi_{MI}$ for three different axial positions of the adjustable probe above the impeller (Re = 32,000); ●: z/T = 0.687; ▷: z/T = 0.625; □: z/T = 0.562.

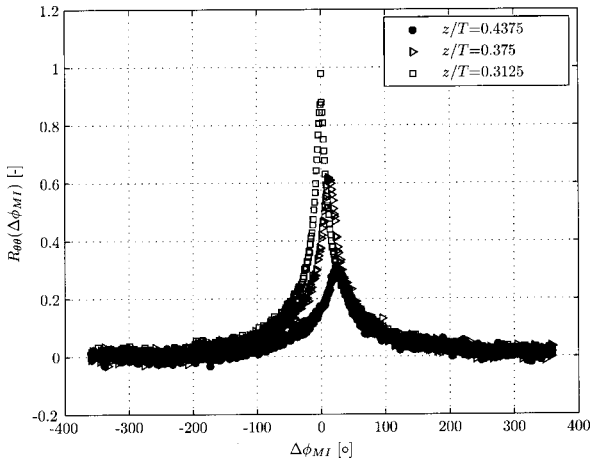

Figure 11. Variation of the correlation coefficient $R_{\theta\theta}$ with phase-lag angle $\Delta\phi_{MI}$ for three different axial positions of the adjustable probe below the impeller (Re = 32,00); ●: z/T = 0.437; ▷: z/T = 0.375; □: z/T = 0.312.

surements taken in the lower part of the vessel, also in this case the phase lag $\Delta\phi_{MI}$ associated to the maximum of $R_{\theta\theta}$ does not change for the different axial positions examined, leading to the conclusion that the axis of the MI vortex above the impeller is also vertical.

The variations of the correlation coefficient $R_{\theta\theta}(\Delta\phi_{MI})$ with phase lag $\Delta\phi_{MI}$ for the axial positions z/T assumed by the adjustable probe below and above the impeller for $Re = 3{,}200$ are shown in Figures 11 and 12, respectively. Considering Figure 11, it is possible to see again that the correlation coefficient maximum decreases with increasing z/T, with values around 1 and 0.3 for positions of the adjustable probe of $z/T = 0.315$, and $z/T = 0.4375$, respectively. In this case however, the $\Delta\phi_{MI}$ associated to the maximum correlation coefficient is different for different z/T, with higher positive values of $\Delta\phi_{MI}$ for increasing z/T. This characteristic indicates that the MI axis is inclined in the $\theta - z$ plane. Considering the definition of $\Delta\phi_{MI}$, positive values of the phase lag, associated with a maximum $R_{\theta\theta}$, indicate that MI vortex exhibits some delay at the axial positions of $z/T = 0.375$–0.437, where the adjustable probe was alternatively located, in comparison to the position $z/T = 0.315$ where the fixed probe was located. This leads to the conclusion that the MI vortex is precessing with axial locations further away from the impeller experiencing its passage in advance of locations nearer the impeller. The inclination of the MI vortex can be estimated by using Eq. (3),

$$\alpha = \tan^{-1}\left(\frac{r\Delta\phi_{MI}}{\Delta z}\right) \tag{3}$$

where r is the radial coordinate of the two probes (that is, $r/T \approx 0.08$). In Eq. (3) α is the angle between the z axis, and the MI axis. Taking into account that $\Delta\phi_{MI} = 23^\circ$ for $z/T = 0.4375$ the inclination of the MI vortex in the $\theta - z$ plane was found to be $\alpha = 14.4^\circ$.

It is interesting that although Figure 11 indicates a 14° inclination of the MI vortex axis below the impeller, there is no correlation with the corresponding locations above $z/T = 0.5$ in Figure 12. The reason for this is thought to be the interference and eventual MI vortex disruption caused by the impeller shaft. In this respect an indication of the MI vortex axis and shape above the impeller centerline, can be obtained by reflecting with respect to the impeller centerline the data (vortex center and diameter) shown in the LHS of Figure 6. In such a case the upper part of the vortex axis (closer to the surface) would be located at r/D around 0.15, that is, very close to the shaft, while in this region the MI radius would encompass the shaft. This implies that the shaft interacts with the vortex for $z/T \geqslant 0.5$, leading to more complex phenomena in such locations, and making the identification of the vortex axis ambiguous. This is indeed thought to be the reason why[15], who deduced the vortex axis location, and number of vortices present from visual observation alone, discerned more than one vortex to be present. Interaction of the MI vortex with the shaft in their case might well have resulted in the appearance of multiple vortices on the liquid surface.

In-vortex tracer insertion and effect on mixing time

Figure 13 shows two different types of mixing time transients one with overshoot, which was found to be consistently present when the insertion was made outside of the vortex core, and a second one without, which was generally (for 80% of the cases) associated to an insertion inside the vortex core. In this respect it should be noted that in both cases (that is, inside and outside of the vortex) the insertion was always made in a region upstream of the conductivity probe, and, therefore, a transient with overshoot is justified by the significant change in tracer concentration taking place in the region of the conductivity probe a few seconds after the insertion. The transient associated to an insertion inside the MI vortex may be due to the tracer being entrained more rapidly and uniformily through its suction to the impeller region. This behavior was clearly visible (as a more opaque tracer cloud) during the insertion when the tracer's dispersion was not as immediate as in the case of an outside vortex insertion. This type of in-vortex transient may be desirable in mixing with chemical reactions, where locally large fluctuations of a reactant volume can lead to unwanted side reactions and by products.

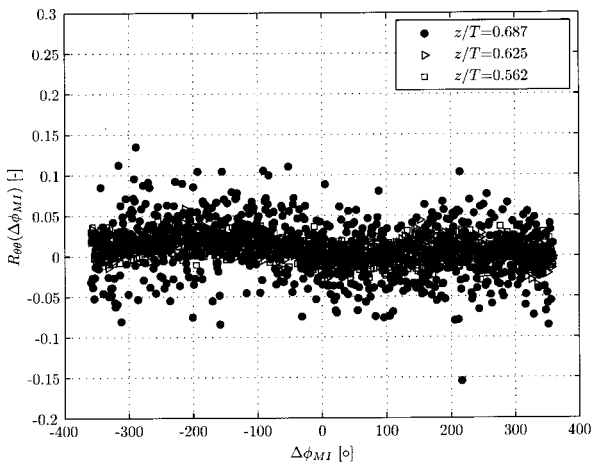

Figure 12. Variation of the correlation coefficient $R_{\theta\theta}$ with phase-lag angle $\Delta\phi_{MI}$ for three different axial positions of the adjustable probe above the impeller (Re = 32,00); ●: z/T = 0.687; ▷: z/T = 0.625; □: z/T = 0.562.

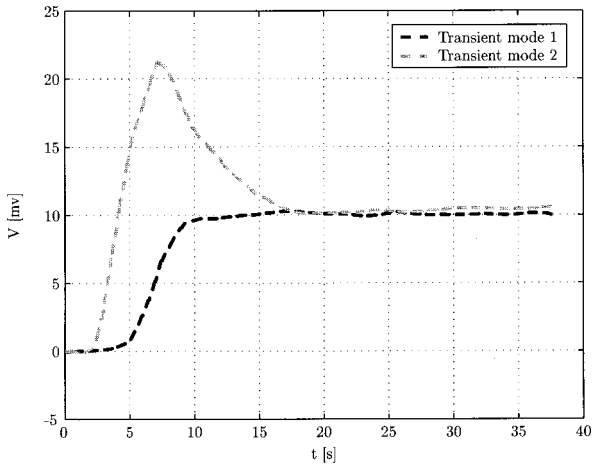

Figure 13. Typical variation of the mixing transients for different modes of insertion: Mode 1, typical for insertions inside the MI vortex; Mode 2, typical for insertions outside of the MI vortex.

The definition of mixing time, θ employed by[32], and calculated according to the average shown in[4] was used

$$\theta = \sum_{i=1}^{13} \frac{\xi_i}{13} \tag{4}$$

where ξ_i are the mixing times for degree of mixing varying from 92% to 98% at intervals of 0.5%. Considering the water height $H/T = 0.75$, preferred in this stage of the work to better visualize the vortex and given the difficulties encountered in identifying in the literature a reference value for the mixing time of the system employed, a first estimate of the mixing time was obtained by using Eq (5) reported in[33]:

$$\theta_{95} = 5.2 \frac{T^{1.5} H^{0.5}}{P_0^{1/3} N D^2} \tag{5}$$

where θ_{95} is the mixing time required to achieve a 95% degree of homogeneity, and P_0 is the power number. Given the generality of the formula of Eq. (5), which is applicable to very different systems (for example, different impellers, geometries, *Re,* and so on), the estimated mixing time, approximately 21 s, is not too different from the averaged one, around 17 s, directly found from all the experiments made, with insertion both inside and outside the vortex core, in this study.

A comparison between the average, $\bar{\theta}$, and standard deviation, θ', of the mixing time estimated from samples associated to an insertion inside and/or outside of the MI vortex is reported in Table 1. As the tabulated data shows, tracer insertion outside the vortex results in mixing times that are around 20% higher than those measured when the tracer is inserted inside the vortex. Similar differences should be expected regardless of the mixing time definition employed (for example, θ_{99} or θ_{95}), as the characteristic mixing curves encountered for the two types of insertion shown in Figure 13 clearly indicate that mixing is achieved faster and the transient exhibits no overshoot for *in vortex* insertion.

Table 1. Comparison of the Mean and Standard Deviation of the Mixing Time θ, Estimated from the Total Number of Samples N_s, and only from Selected Samples Associated to an Insertion Inside and/or Outside of the MI Vortex

	Insertion		
	Tot	in	Out
$\bar{\theta}$ [s]	16.9	15.3	18.2
θ' [s]	3.1	2.4	1.7
N_s [−]	103	59	44

The pdf's with associated Gaussian curves for the inside and outside the vortex insertions are shown in Figure 14. The difference in mean and standard deviation is evident with a narrower Gaussian distribution associated with outside vortex insertions that are clearly related to a better repeatability of this type of insertion. From this point of view, it must be emphasized that in-vortex insertion in the present work was achieved through visual observation of the vortex passage on the liquid surface past the tracer feed tube, and this might have resulted in some of these insertions being made very close to but not strictly within the vortex. This may be the reason for at least some of the higher mixing time values recorded for the *in vortex* case in Figure 14. It is not unreasonable to expect that with a more accurate means of insertion synchronization with the vortex passage (for example, by employing a pressure transducer in the manner of[12] and a multihole insertion tube of larger area), the mixing-time distributions should be more akin to the dashed lines shown in Figure 14. If this is indeed the case, then the average mixing time would be reduced from around 18 to around 14 s, or by approximately 30%.

Finally a *t*-test was carried out between the two groups of data (that is, associated to an insertion inside or outside of the vortex) to assess whether they are statistically different from each other. The t-test was implemented by applying Eq. 6 (see for example[34])

$$t = \frac{\bar{\theta}_{out} - \bar{\theta}_{in}}{\sqrt{\frac{\theta'^2_{in}}{N_{s_{in}}} + \frac{\theta'^2_{out}}{N_{s_{out}}}}} \tag{6}$$

where the suffices *in* and *out* refer to characteristics associated to an insertion inside and outside of the vortex. The value of

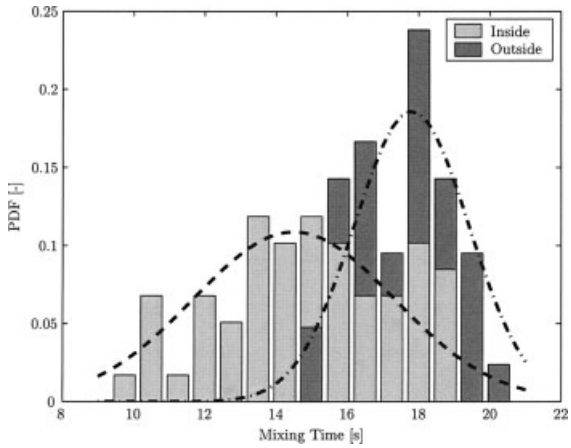

Figure 14. Probability distributions of mixing time measurements; light gray: insertion inside the MI vortex; dark gray: insertion outside MI vortex.

t (5.32) determined from Eq. 6 is higher than the tabulated value of 1.98 reported by[34] for a Student t distribution, indicating that the groups are statistically different with a 95% level of confidence.

Conclusions and Implications for Mixing Practice

The present investigation has provided results of both fundamental and applied significance. The combination of the PIV and LDA optical techniques has provided, hitherto, unavailable information on the structure, location, extent and strength of the MI vortices in stirred vessels for both low and high *Re* flows. Importantly, these findings complement the work of[15] as they have not only confirmed that one reason for the different f' values exhibited in the two *Re* cases is indeed the difference in the radius of the vortex axis, but have also shown that another reason is the difference in flow structure and not the number of MI vortices present in the low-Re case.

The knowledge of the vortex path obtained has guided the location of the tracer insertion for mixing time measurements that indicated considerable (20% and possibly 30%) reduction in mixing time, and, consequently, a similar decrease in the power consumed for a mixing task. Future work will aim to utilize the knowledge of average vortex size and vortex axis location obtained in this work, in conjunction with a pressure transducer to trigger tracer insertion in synchronization with the vortex passage in a particular radial plane and a multihole insertion tube to achieve *in vortex* insertion more consistently. An immediate estimate of the efficiency of such a system can be made by considering the pdf's shown in Figure 5 where a multihole insertion tube with a diameter of around 0.2 D located at a radius of 0.33 D would increase the probability of a correct *in vortex* insertion of a second phase to 65–70% of vortex occurrences. This proposed approach should be readily transferable to industrial mixing vessels to achieve mixing enhancement in practical mixing systems.

The work reported here has indicated the advances in process design and efficiency that might be achieved through an improved understanding of the fundamentals of the fluid mechanics of stirred vessels, and bodes well for the further optimization of mixing processes.

Notation

Abbreviation

LDA = laser doppler anemometer
LES = large eddy simulation
LHS = lefthand side
MI = macroinstability
PIV = particle-image velocimeter
RHS = right hand side

Greek letters

α = inclination of the vortex in the $z-\theta$ plane, $^\circ$
Δz = displacement in the z direction, m
$\Delta\phi_{MI}$ = phase lag, $^\circ$
θ = mixing time of a singular insertion, s
$\underline{\theta}$ = tangential coordinate,
$\bar{\theta}$ = average mixing time of N_s insertions, s
λ = generic eigenvalue of the tensor $S^2+\Omega^2$, s^{-2}.
λ_2 = second highest eigenvalue of the tensor $S^2+\Omega^2$, s^{-2}
ρ = instantaneous MI vortex radius, m
$\bar{\rho}$ = ensemble averaged vortex MI radius, m
ϕ_{MI} = phase angle accounting for the extent of precession of the MI vortex, $^\circ$
Ω = rotation rate tensor, s^{-1}
ω = angular velocity of the solid body rotation region, rad s^{-1}
ω_z = vorticity in the axial direction, s^{-1}
$\bar{\omega}_z$ = ensemble averaged vorticity in the axial direction, s^{-1}

Roman symbols

C = Impeller clearance, m
C_{x_i} = coordinate in the x_i direction of the vortex center, m
D = impeller diameter, m
f = precessional frequency of the MI vortex, s^{-1}
f' = precessional frequency of the MI vortex non-dimensionalized by N
H = water height, m
N_s = number of samples
P_o = power number
p = pressure, Kg $s^{-2}m^{-1}$
r = radial coordinate, m
Re = Reynolds number
$R_{\theta\theta}$ = correlation of the velocity component in the θ direction
S = deformation rate tensor, s^{-1}
T = vessel diameter, m
T_{MI} = period of precession of the MI vortex, s
t = particle arrival time, s
U_i = velocity in the i_{th} direction, ms^{-1}
v_{tip} = Velocity of the tip of the blade, ms^{-1}
x_i^* = i_{th} eigenvector of the tensor $S^2+\Omega^2$, s^{-2}, m
z = axial coordinate, m

Literature Cited

1. van't Riet K, Smith J. The trailing vortex system produced by Rushton turbine agitators. *Chem Eng Sci*. 1975;30:1093–1105.
2. Yianneskis M, Popiolek Z, Whitelaw JH. An experimental study of the steady and unsteady flow characteristics of stirred reactors. *J Fluid Mech*. 1987;175:537–555.
3. Yoon H, Sharp K, Hill D, Adrian R, Balachandar S, Ha M, Kar K. Integrated experimental and computational approach to simulation of flow in a stirred tank. *Chem Eng Sci*. 2001;56(23):6635–6649.
4. Escudié R, Buoyer D, Line A. Characterization of trailing vortices generated by a Rushton turbine. *AIChE J*. 2004;50(1):75–85.
5. Yoon H, Hill D, Balachandar R, Adrian S, Ha M. Reynolds number scaling of flow in a rushton turbine stirred tank. part i - mean flow, circular jet and tip vortex scaling. *Chem Eng Sci*. 2005;60(12):3169–3183.
6. Nikiforaki L, Montante G, Lee KC, Yianneskis M. On the origin, frequency and magnitude of macro-instabilities of the flows in stirred vessels. *Chem Eng Sci*. 2003;58:2937–2949.
7. Galletti C, Paglianti A, Yianneskis M. Observations on the significance of instabilities, turbulence and intermittent motions on fluid mixing processes in stirred reactors. *Chem Eng Sci*. 2005;60:2317–2331.
8. Escudié R, Liné A. Experimental analysis of hydrodynamics in a radially agitated tank. *AIChE J*. 2003;49(3):585–603.
9. Ducci A, Yianneskis M. Direct determination of energy dissipation in stirred vessels with two-point LDA. *AIChE J*. 2005;51(8):2133–2148.
10. Montes J, Boison H, Fort I, Jahoda M. Velocity field macro-instabilities in an axially agitated mixing vessel. *Chem Eng J*. 1997;67:139–145.
11. Roussinova V, Kresta S, Weetman R. Low frequency macroinstabilities in a stirred tank: scale up and prediction based on large eddy simulations. *Chem Eng Sci* 2003;58:2297–2311.
12. Paglianti A, Montante G, Magelli F. Novel experiments and a mechanics model for macoinstabilities in stirred tanks. *AIChE J*. 2006;52(2):426–437.
13. Larsson G, Tornkvist M, Stahl Wernersson E, Tragardh K, Noorman H, Enfos S. Substrate gradients in bioreactors: origin and consequences. *Bioprocess Eng*. 1996;14:281–289.
14. Grosjean N, Graftieaux L, Michard M, Hubner W, Tropea C. Combining PDA and PIV for turbulence measurements in unsteady swirling flows. *Exp Fluids*. 1997;8:1523–1532.

15. Galletti C, Paglianti A, Lee KC, Yianneskis M. Reynolds number and impeller diameter effects on instabilities in stirred vessels. *AIChE J*. 2004;50:2050–2063.
16. Serre E, Bontoux P. Three-dimensional swirling flow with a precessing vortex breakdown in a rotor-stator cylinder. *Phys Fluids*. 2001; 13:3500–3503.
17. Escudier M. Confined vortices in flow machinery. *Ann Rev Fluid Mech*. 1987;19:27–52.
18. Ducci A, Yianneskis M. Analysis of errors in the measurement of energy dissipation with two-point LDA. *Exp Fluids*. 2005;38:449–460.
19. Gibson C, Schwarz W. Detection of conductivity fluctuations in a turbulent flow field. *J Fluid Mech*. 1963;16:357–364.
20. Ruszkowski S. A rational method for measuring the blending performance and comparison of different impeller types. *IChemE Symp Series* 1994;136:283–291.
21. Micheletti M, Nikiforaki L, Lee K, Yianneskis M. Particle concentration and mixing characteristics of moderate to dense solid-liquid suspensions. *Ind Eng Chem Res*. 2003;42:6236–6249.
22. Nouri J, Whitelaw JH, Yianneskis M. An experimental study of the steady and un- steady flow characteristics of stirred reactors. *Proc. 2nd international conference on laser anemometry-advances and applications*. Glasgow; 21–23 Sept. 1987;175:489–500.
23. Rutherford K. Hydrodynamic characteristics of stirred vessels with single and multiple impellers. King's College London, University of London, U.K. 1997; Ph.D. Thesis.
24. Ducci A, Yianneskis M. Vortex identification methodology for feed insertion guidance in fluid mixing processes. *Trans IChemE Chem Eng Res Des*. 2007; In press.
25. Jeong J, Hussain F. On the identification of a vortex. *J. Fluid Mech*. 1995;285:69–94.
26. Bradshaw P, Koh W. Particle concentration and mixing characteristics of moderate to dense solid-liquid suspensions. *Phys Fluids*. 1981;24(4):777.
27. Cantwell B, Coles D. An experimental study of entrainment and transport in the turbulent near wake of a circular cylinder. *J Fluid Mech*. 1983;136:321–374.
28. Wu H, Patterson GK. Laser-Doppler measurements of turbulent-flow parameters in a stirred mixer. *Chem Eng Sci*. 1989;44(10):2207–2221.
29. Stoots C, Calabrese R. The mean velocity field relative to a Rushton turbine blade. *AIChE J*. 1994;41:1–11.
30. Lee KC, Yianneskis M. Turbulence properties of the impeller stream of a Rushton turbine. *AIChE J*. 1998;44(1):13–24.
31. Micheletti M, Yianneskis M. Precessional flow macro-instabilities in stirred vessels: study of variation in two locations through conditional phase averaging and cross correlation approach. *Proc. 11th Int. Symp. on Applications of Laser techniques to Fluids Mechanics*. Lisbon, Portugal; Paper: 19.2. 2002.
32. Mahmoudi S. Velocity and mixing characteristics of stirred vessels with two Rushton impellers, King's College London, University of London, U.K. (1994). Ph.D. thesis.
33. Grenville R. Blending of viscous Newtonian and pseudo-plastic fluids, Ph.D. thesis, Cranfield Institute of Technology, U.K.; 1992.
34. Bendat JS, Piersol AG. Random data: analysis and measurement procedures. 2nd Ed. Wiley Interscience; 1987.

Manuscript received Jun. 21, 2006, and revision received Oct. 18, 2006.